Journal of Physics D: Applied Physics

PAPER • **OPEN ACCESS**

Field- and temperature-modulated spin diode effect in a GMR nanowire with dipolar coupling

To cite this article: Piotr Ogrodnik *et al* 2019 *J. Phys. D: Appl. Phys.* **52** 065002

View the article online for updates and enhancements.

IOP ebooks™

Bringing together innovative digital publishing with leading authors from the global scientific community.

Start exploring the collection–download the first chapter of every title for free.

This content was downloaded from IP address 128.178.141.41 on 30/04/2021 at 10:58

OPEN ACCESS
IOP Publishing
Journal of Physics D: Applied Physics
J. Phys. D: Appl. Phys. **52** (2019) 065002 (13pp)
https://doi.org/10.1088/1361-6463/aaf093

Field- and temperature-modulated spin diode effect in a GMR nanowire with dipolar coupling

Piotr Ogrodnik[1,2], Francesco Antonio Vetrò[3], Marek Frankowski[1], Jakub Chęciński[1,4], Tomasz Stobiecki[1,4], Józef Barnaś[5,6] and Jean-Philippe Ansermet[3]

[1] Department of Electronics, AGH University of Science and Technology, Al. Mickiewicza 30, 30-059 Kraków, Poland
[2] Faculty of Physics, Warsaw University of Technology, ul. Koszykowa 75, 00-662 Warszawa, Poland
[3] École Polytechnique Fédérale de Lausanne—EPFL, Institute of Physics, Station 3, CH-1015 Lausanne, Switzerland
[4] Faculty of Physics and Applied Computer Science, AGH University of Science and Technology, Al. Mickiewicza 30, 30-059 Kraków, Poland
[5] Faculty of Physics, Adam Mickiewicz University, ul. Umultowska 85, 61-614 Poznań, Poland
[6] Polish Academy of Sciences, Institute of Molecular Physics, ul. M. Smoluchowskiego 17, 60-179 Poznań, Poland

E-mail: piotrogr@if.pw.edu.pl

Received 2 July 2018, revised 24 October 2018
Accepted for publication 13 November 2018
Published 30 November 2018

Abstract

The magnetization dynamics of single Co/Cu/Co spin valves, embedded in electrodeposited nanowires of 30 nm avarage diameter, was observed using the spin-diode effect. The electrically-detected magnetic resonances were compared when using modulation of either the magnetic field or a laser irradiation. The effect of temperature modulation was accounted for by introducing the temperature dependence of the saturation magnetization and anisotropy, as well as thermal spin-transfer torque (TSTT). The predictions of the model are compared with experimental data. Two forms of modulation give rise to qualitative differences in the spectra that are accounted for by the model only if both temperature-modulated magnetization and TSTT are introduced in the model. On the contrary, the temperature modulation of the magnetic anisotropy has a smaller contribution.

Keywords: nanowires, spin diode effect, GMR, dipolar coupling, STT, heat-driven STT

(Some figures may appear in colour only in the online journal)

1. Introduction

The spin diode effect (SDE) is a well established method of electrical detection of magnetic dynamics in ferromagnetic layers [1–8]. The effect occurs when an alternating current (*AC*) passes through a magnetic structure and excites oscillations of the magnetization vector. This, in turn, leads to variation of the resistance due to the magnetoresistance effect. The oscillating resistance can then mix with the *AC* current to produce a direct (*DC*) output voltage, V_{DC}. The SDE is of great importance from the point of view of further development of magnetic sensors, microwave communication and ultrafast electronics—especially since the nanostructures manufactured nowadays make it possible to get smaller and more efficient electronics elements [5, 8, 9].

Until now, the SDE was investigated mainly in systems with one ferromagnetic free layer (see the review paper by Harder *et al* [7]). Although more ferromagnetic layers were present in

Original content from this work may be used under the terms of the Creative Commons Attribution 3.0 licence. Any further distribution of this work must maintain attribution to the author(s) and the title of the work, journal citation and DOI.

some devices, they were usually assumed to be magnetically stiff (pinned layers). However, in some of the experimentally investigated structures there were two or more magnetically free layers that, in addition, were dynamically coupled by the RKKY-like exchange interaction or by dipolar interactions [9–13]. Moreover, they were also dynamically coupled by spin transfer torque (STT) effects [14]. Nevertheless, most of these devices with multiple free magnetic layers, still included at least one, usually thick, pinned magnetic polarizer [15, 16].

Regardless of its source, the coupling between layers may lead, in general, to more complex magnetization dynamics and a non-trivial behaviour of the device. Particularly, it is important when ultrafast magnetic dynamics is studied in terms of the SDE with different experimental (field or temperature) modulation techniques. In this paper we address this problem. Our analytical model is based on the Landau–Lifschitz–Gilbert–Slonczewski (LLGS) equation [17] and accounts for two dynamic coupling: the spin transfer torque effect and the dipolar interactions between two magnetically free layers of a GMR spin valve (GMR-SV) embbeded in a nanowire. The model is applied to SDE spectra in this specific system, especially to reproduce and explain the qualitative differences observed when the ferromagnetic resonance spectra are measured under field or temperature modulation. We analyse in detail the influence of the type of modulation technique on the shape of the resonance spectra. When considering the laser modulation technique, we assume a temperature dependence of the saturation magnetization and anisotropy parameters. Also we consider the presence of thermal STTs (TSTTs) [18] due to temperature gradient generated along the nanowire [19]. Recently, the TSTT has been considered theoretically [20] as well as observed experimentally in the metallic spin-valves [21, 22] and also in magnetic tunnel juntions [23, 24]. Apart from this, the SDE has been applied to analyse the line-shape evolution due to TSTT in a standard magnetic tunnel junction with a single free layer [25].

The Co/Cu/Co nanowires were fabricated by electrochemical deposition technique with diameters of about 30 nm. In such structures there is a strong dipolar coupling between the Co layers. To support our analytical calculations based on the macrospin model, we also performed micromagnetic simulations.

The paper is organized as follows. In section 2 we present a theoretical description of the magnetization dynamics in the system and also describe briefly the spin diode effect. In section 3 the experimental part is presented. In section 4 we discuss results for the V_{DC} signal and line shapes in the case of field and laser modulation techniques. Summary and final conclusions are given in section 5.

2. Theoretical description

In this section we present a theoretical description of SDE in the case of two magnetic layers which are dynamically coupled by a dipolar field and STT effects. The system under considerations consists of two magnetic (Co) layers of circular

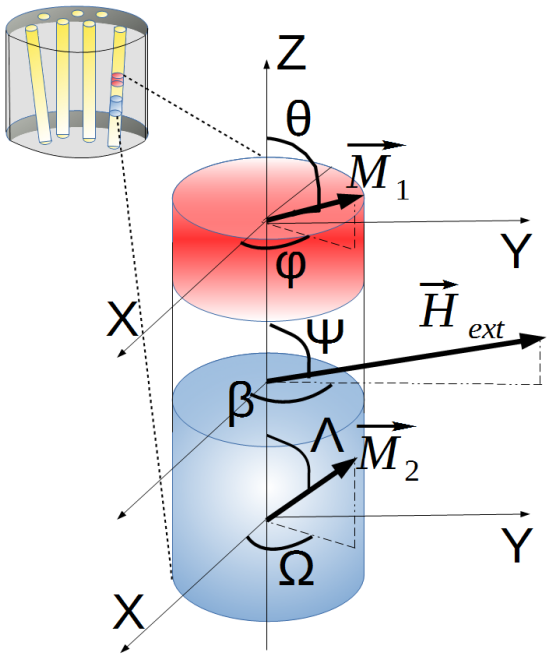

Figure 1. Schematics of the GMR-SV embedded in a single nanowire which is considered in this paper. Nanowires are deposited within polycarbonate membrane, schematically depicted as grey strainer-like structure. Magnetic moments of the top (thin) and bottom (thick) layers of SV are described by the angles (θ, ϕ) and (Λ, Ω), respectively. The orientation of the external magnetic field $\boldsymbol{H}_{ext}$ (acting on both layers) is described by the angles Ψ and β.

shape, which are separated by a non-magnetic (Cu) layer. The geometry of the nanowire is shown schematically in figure 1.

In order to simulate the SDE, we need to consider first the magnetic dynamics in the system, driven by an *AC* charge current flowing along the wire. The dynamics may be induced by a time-dependent STT and by time-dependent Oersted field, both being associated with the *ac* current. The magnetic moment in each layer is described by the corresponding polar and azimuthal angles,

$$\boldsymbol{M}_1 = M_{S,1}[\sin\theta\cos\phi, \sin\theta\sin\phi, \cos\theta] \tag{1}$$

for the thinner layer, and

$$\boldsymbol{M}_2 = M_{S,2}[\sin\Lambda\cos\Omega, \sin\Lambda\sin\Omega, \cos\Lambda] \tag{2}$$

for the thicker magnetic layer. Here, $M_{S,1}$ and $M_{S,2}$ are the saturation magnetizations of the thin and thick magnetic layers, respectively.

The magnetization dynamics of the system is described by two coupled Landau–Lifshitz–Gilbert–Slonczewski equations,

$$\frac{d\boldsymbol{M_1}}{dt} = -\gamma_e \boldsymbol{M_1} \times \boldsymbol{H}_{\mathrm{eff},1} + \frac{\alpha_1}{M_{S,1}} \boldsymbol{M_1} \times \frac{d\boldsymbol{M_1}}{dt} + \gamma_e \boldsymbol{\tau_1}, \tag{3a}$$

$$\frac{d\boldsymbol{M_2}}{dt} = -\gamma_e \boldsymbol{M_2} \times \boldsymbol{H}_{\mathrm{eff},2} + \frac{\alpha_2}{M_{S,2}} \boldsymbol{M_2} \times \frac{d\boldsymbol{M_2}}{dt} + \gamma_e \boldsymbol{\tau_2}, \tag{3b}$$

where γ_e stands for the gyromagnetic ratio, while α_1 (α_2) and $\boldsymbol{\tau_1}(\boldsymbol{\tau_2})$ denote the Gilbert damping parameters and STT

vectors acting on the thin(thick) magnetic layer respectively. In general case, the effective fields may be written as a sum of gradient of total magnetic energy density U and Oersted field (see appendix). Since we do not consider the Oersted field throughout the paper, we express the effective fields as follows:

$$\boldsymbol{H}_{\mathrm{eff},1} = -\boldsymbol{\nabla}_{\theta,\phi} U \tag{4a}$$

$$\boldsymbol{H}_{\mathrm{eff},2} = -\boldsymbol{\nabla}_{\Lambda,\Omega} U, \tag{4b}$$

where $\boldsymbol{\nabla}_{\theta,\phi}$ and $\boldsymbol{\nabla}_{\Lambda,\Omega}$ stand for the relevant gradients in spherical coordinates.

The total magnetic energy density U can be written as

$$\begin{aligned} U(\theta,\phi,\Lambda,\Omega) &= K_1(\cos^2\theta + \sin^2\theta\sin^2\phi) - \boldsymbol{M_1}\cdot\boldsymbol{H}_{\mathrm{ext}} \\ &- \boldsymbol{M_1}\cdot\boldsymbol{H}_{dem,1} + K_2(\cos^2\Lambda + \sin^2\Lambda\sin^2\Omega) - \boldsymbol{M_2}\cdot\boldsymbol{H}_{\mathrm{ext}} \\ &- \boldsymbol{M_2}\cdot\boldsymbol{H}_{\mathrm{dem},2} - \boldsymbol{M_1}\cdot\boldsymbol{H}_{\mathrm{dip},2} - \boldsymbol{M_2}\cdot\boldsymbol{H}_{\mathrm{dip},1}, \end{aligned} \tag{5}$$

where K_1 and K_2 are the magnetocrystalline anisotropy constants of the thin and thick layers, respectively, $\boldsymbol{H}_{\mathrm{ext}}$ is an external magnetic field, $\boldsymbol{H}_{\mathrm{dem},1}$ and $\boldsymbol{H}_{\mathrm{dem},2}$ are the demagnetizing fields within the thin and thick layers, while $\boldsymbol{H}_{\mathrm{dip},2}$ and $\boldsymbol{H}_{\mathrm{dip},1}$ are the respective dipolar fields. Demagnetizing fields can be also expressed by demagnetizing tensors, i.e. $\boldsymbol{H}_{\mathrm{dem},1} = \hat{N}_1 \cdot \frac{\boldsymbol{M_1}}{\mu_0}$ and $\boldsymbol{H}_{\mathrm{dem},1} = \hat{N}_2 \cdot \frac{\boldsymbol{M_1}}{\mu_0}$, which can be calculated analytically for each layer [26].

Assuming uniform magnetization within both magnetic layers, one can estimate the magnitude of the interaction between the layers due to dipolar fields by taking into account the field calculated directly at the geometrical center of each layer. Then, the magnetic moment $\boldsymbol{m}$ within volume dV generates the magnetic field that may be expressed as follows:

$$d\boldsymbol{H}_{dip} = \frac{1}{\mu_0}\frac{M_S}{4\pi}\left(\frac{3\hat{\boldsymbol{n}}\cdot(\hat{\boldsymbol{m}}\cdot\hat{\boldsymbol{n}}) - \hat{\boldsymbol{m}}}{\mathcal{R}^3}\right). \tag{6}$$

Here, μ_0 stands for vacuum permeability, $\boldsymbol{\mathcal{R}}$ denotes the position vector connecting the volume dV within one magnetic layer and the geometrical center of second layer, while the unit vector $\hat{\boldsymbol{n}}$ is defined as $\hat{\boldsymbol{n}} = \boldsymbol{\mathcal{R}}/\mathcal{R}$. Upon integrating the above equation over the volume of the whole layer, one finds the dipolar field at any point on the axis z:

$$H_{dip,i}(z) = \int_0^{2\pi} d\phi \int_0^{d} dz' \int_0^{R} d\rho'\rho' dH_{dip,i} \tag{7}$$

for $i \equiv x, y, z$, where d and R denote the thickness and radius of the corresponding layer. The above integral may be calculated analytically in our case. This approach allows us to calculate dipolar fields in an efficient way without significant overestimations.

Each of the STTs acting on the two magnetic layers, $\boldsymbol{\tau}_1$ and $\boldsymbol{\tau}_2$, consists of two terms, $\boldsymbol{\tau}_1 = \boldsymbol{\tau}_{\parallel,\mathbf{1}} + \boldsymbol{\tau}_{\perp,\mathbf{1}}$, and similarly for $\boldsymbol{\tau_2}$. These two components can be written as

$$\boldsymbol{\tau}_{\parallel,\mathbf{1}} = \tau_{\parallel,1}(\hat{\boldsymbol{m}}_\mathbf{1}\times\hat{\boldsymbol{m}}_\mathbf{2}\times\hat{\boldsymbol{m}}_\mathbf{1}), \tag{8a}$$

$$\boldsymbol{\tau}_{\perp,\mathbf{1}} = \tau_{\perp,1}(\hat{\boldsymbol{m}}_\mathbf{1}\times\hat{\boldsymbol{m}}_\mathbf{2}), \tag{8b}$$

and

$$\boldsymbol{\tau}_{\parallel,\mathbf{2}} = \tau_{\parallel,2}(\hat{\boldsymbol{m}}_\mathbf{2}\times\hat{\boldsymbol{m}}_\mathbf{1}\times\hat{\boldsymbol{m}}_\mathbf{2}), \tag{9a}$$

$$\boldsymbol{\tau}_{\perp,\mathbf{2}} = \tau_{\perp,2}(\hat{\boldsymbol{m}}_\mathbf{2}\times\hat{\boldsymbol{m}}_\mathbf{1}), \tag{9b}$$

where $\hat{\boldsymbol{m}}_\mathbf{1}$ and $\hat{\boldsymbol{m}}_\mathbf{2}$ are unit vectors along the magnetic moments, $\hat{\boldsymbol{m}}_\mathbf{1} = \boldsymbol{M}_1/M_{S,1}$ and $\hat{\boldsymbol{m}}_\mathbf{2} = \boldsymbol{M_2}/M_{S,2}$.

The first components (equations (8*a*) and (9*a*)) have the form of damping/antidamping torque and are also frequently described as the in-plane components, because the torque is in the plane determined by the two magnetic moments. The second components (equations (8*b*) and (9*b*)) are known as the field-like torques as their form is similar to that of the field-generated torque, i.e. the torque is perpendicular to the plane determined by m_1 and m_2. In metallic systems the field-like torque is usually smaller than the damping/antidamping one, thus we can neglect this component in our calculations. Apart from this, the scalar amplitudes $\tau_\parallel$ and $\tau_\perp$ may be generally angle dependent due to spin accumulation in the GMR structures [27]. In our case, the STT plays the role of an *ac* driving force and thus a more complex angular dependence of STT does not lead to significant modifications of the spin diode lineshape or resonance frequency.

Since the induced oscillations of $\boldsymbol{M}_1$ and $\boldsymbol{M_2}$ around the equilibrium positions can be assumed as small ones, the LLGS equation (3) can be linearized and then its solution can be expressed as harmonic oscillations of magnetization angles in polar coordinates, i.e.

$$\theta(t) = \theta_0 + \delta\theta(t) = \theta_0 + \delta\theta e^{i(\omega t+\Psi_1)}, \tag{10a}$$

$$\phi(t) = \phi_0 + \delta\phi(t) = \phi_0 + \delta\phi e^{i(\omega t+\Psi_2)}, \tag{10b}$$

$$\Lambda(t) = \Lambda_0 + \delta\Lambda(t) = \Lambda_0 + \delta\Lambda e^{i(\omega t+\Psi_3)}, \tag{10c}$$

$$\Omega(t) = \Omega_0 + \delta\Omega(t) = \Omega_0 + \delta\Omega e^{i(\omega t+\Psi_4)}, \tag{10d}$$

where (θ_0, ϕ_0) and (Λ_0, Ω_0) describe the equilibrium orientation of the magnetization in the thin and thick layers (in the absence of the *ac* driving current), whereas (Ψ_1, Ψ_2) and (Ψ_3, Ψ_4) account for the phase shifts in the two magnetic layers between the *ac* current and driving force. The small deviations $(\delta\theta, \delta\phi)$ and $(\delta\Lambda, \delta\Omega)$ of the angles from the corresponding equilibrium values are generally complex and include the phase shift between the magnetic dynamics and the driving force. The solutions of the LLGS equation, given in the form of equations (10*a*)–(10*d*), can be combined and expressed as one vector $\boldsymbol{\alpha} \equiv (\theta(t), \phi(t), \Lambda(t), \Omega(t))^T$, so that the LLGS equation in polar coordinates has the general form:

$$\dot{\boldsymbol{\alpha}} = \boldsymbol{\nu}(\theta,\phi,\Lambda,\Omega)^T \tag{11}$$

where $\boldsymbol{\nu}$ is RHS vector of the LLGS equation (see equation (A.5) in appendix). After linearization of $\boldsymbol{\nu}$ with respect to small changes of the *ac* voltage, $\delta V(t)$, and small deviations

of $\theta, \phi, \Lambda, \Omega$ from the corresponding stationary values, one can write equation (11) in the form

$$\dot{\boldsymbol{\alpha}} = \hat{X}\boldsymbol{\Gamma}(t) + \boldsymbol{Y}\delta V(t) \tag{12}$$

where $\hat{X}$ is the 4×4 matrix consisting of the derivatives of RHS of equation (11) with respect to the angles $\theta, \phi, \Lambda, \Omega$, i.e. $X_{ij} \equiv \frac{\partial v_i}{\partial \alpha_j}$, while $\boldsymbol{\Gamma}(t) = (\delta\theta(t), \delta\phi(t), \delta\Lambda(t), \delta\Omega(t))^T$ is a vector containing time-dependent angles differentials as defined in equations (10*a*)–(10*d*). The vector $\boldsymbol{Y}$ is composed of the derivatives of RHS of equation (11) with respect to the voltage V.

In the absence of an applied voltage, the second term on the RHS of equation (12) vanishes, and the solutions have the form of damped oscillations. Then, in order to calculate resonance frequencies, one can rewrite equation (12) as an eigenvalue problem of the matrix $\hat{X}$, i.e.

$$|\hat{X} - \lambda\hat{I}| = 0. \tag{13}$$

The eigenvalues λ determine the resonance frequencies of the system, $\omega_i = \Im\lambda$. Since the magnetic moment of each magnetic layer is described by two equations in polar coordinates, the matrix $\hat{X}$ has only two different eigenfrequencies.

Now we find from equation (11) a general solution for $\delta\theta$, $\delta\phi$, $\delta\Lambda$ and $\delta\Omega$ in the presence of applied *ac* voltage. To do this we rewrite equation (11) in matrix form as

$$\hat{B}\,\hat{\Psi}\,\boldsymbol{\Gamma}e^{i\omega t} = \boldsymbol{Y}\,\delta V e^{i\omega t}, \tag{14}$$

where $\hat{B} = i\omega\hat{I} - \hat{X}$, $\hat{\Psi} \equiv \mathrm{diag}(e^{i\Psi_1}, e^{i\Psi_2}, e^{i\Psi_3}, e^{i\Psi_4})$ and time-independent vector of angle amplitudes, $\boldsymbol{\Gamma} \equiv (\delta\theta, \delta\phi, \delta\Lambda, \delta\Omega)^T$. After dividing both sides of the above equation by the oscillating term $e^{i\omega t}$, one obtains a set of linear equations for $\delta\theta, \delta\phi, \delta\Lambda, \delta\Omega$ (or for the vector $\boldsymbol{\Gamma}$), from which one finds $\boldsymbol{\Gamma}$ in the form

$$\boldsymbol{\Gamma} = \left(\hat{B}\,\hat{\Psi}\right)^{-1} \boldsymbol{Y}\,\delta V. \tag{15}$$

Finally, we replace $\boldsymbol{\Gamma}$ by its real part $\Re\{\boldsymbol{\Gamma}\}$.

Having found the general formulas describing magnetization dynamics, we can now determine the spin diode voltage V_{DC} and the lineshape of the spin diode signal. First, we recall that the resistance of a GMR spin valve depends on the angle ξ between magnetizations $\boldsymbol{M_1}$ and $\boldsymbol{M_2}$ as $R(\xi) = R_P + \Delta R(1 - \cos\xi)/2$, where R_P is the resistance in the parallel configuration, while $\Delta R = R_{AP} - R_P$ is the difference in resistance of antiparallel (AP) and parallel (P) configurations. Thus, the spin-diode signal for the GMR nanowire can be expressed by a small change $\delta\xi$ of the angle ξ, which is induced by magnetic dynamics. Accordingly, we write the spin-diode signal as [6]:

$$V_{DC} = \frac{1}{2} I\,\delta R, \tag{16}$$

where I is the amplitude of *ac* current, while δR is the amplitude of resistance change,

$$\delta R(\xi) = \frac{\Delta R}{2}\sin\xi\delta\xi. \tag{17}$$

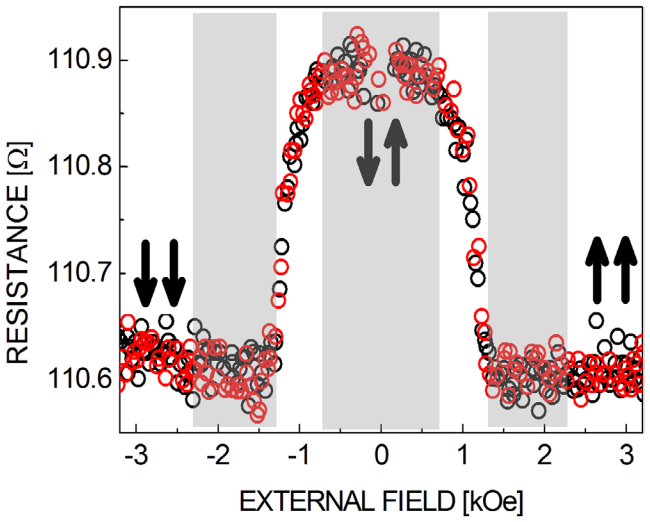

Figure 2. A typical nanowire magnetoresistance curve as a function of magnetic field. Red and black points correspond to sweeping the magnetic field from negative to positive values and vice versa, while black arrows point out the antiparallel (R_{AP}) and parallel (R_P) magnetization orientation of the spin valve. The shaded area indicates the range of magnetic fields where ferromagnetic resonance was driven and analysed (see section 4 for further details).

The angle $\xi = \arccos(\hat{\boldsymbol{m}}_1 \cdot \hat{\boldsymbol{m}}_2)$ can be considered as a function of the angles θ, ϕ, Λ, and Ω. Due to magnetization dynamics, the angles $\theta, \phi, \Lambda, \Omega$ change by $\delta\theta$, $\delta\phi$, $\delta\Lambda$ and $\delta\Omega$, respectively. Thus, the change of ξ due to small changes of the angles $\theta, \phi, \Lambda, \Omega$ can be written as

$$\delta\xi = \left(\frac{\partial\xi}{\partial\theta}, \frac{\partial\xi}{\partial\phi}, \frac{\partial\xi}{\partial\Lambda}, \frac{\partial\xi}{\partial\Omega}\right) \cdot \boldsymbol{\Gamma}. \tag{18}$$

The above equation, together with the equations (17) and (15) for $\delta\theta$, $\delta\phi$, $\delta\Lambda$, and $\delta\Omega$, is sufficient to find the spin diode signal (16). Since the solution for spin diode signal includes the dynamical matrix $\hat{X}$, the V_{DC} signal can be enhanced when the driving force (represented by the vector $\boldsymbol{Y}$) matches the natural frequencies calculated from equation (13)

3. Experimental

To perform measurements of the V_{DC} signal in a GMR system with two magnetically free layers, we prepared asymmetric spin valves consisting of two layers of cobalt, one thicker and one thinner, separated by a copper layer (see figure 1). A standard electrodeposition process in commercial ion-track etched polycarbonate membranes was used. The membrane was 5 μm thick and contained nanopores of 30 nm in diameter with a pore density of 6×10^6 cm^{-2}. Details of the methods for growing and contacting the nanowires were similar to those described in [22, 28, 29]. The typical average value of magnetoresistance increment (ΔR) of these spin valve nanowires amounts to approximately 0.3Ω. The membrane was placed on top of the central conductor of an SMA connector. A shorting plug was mounted on the connector that contained a screw

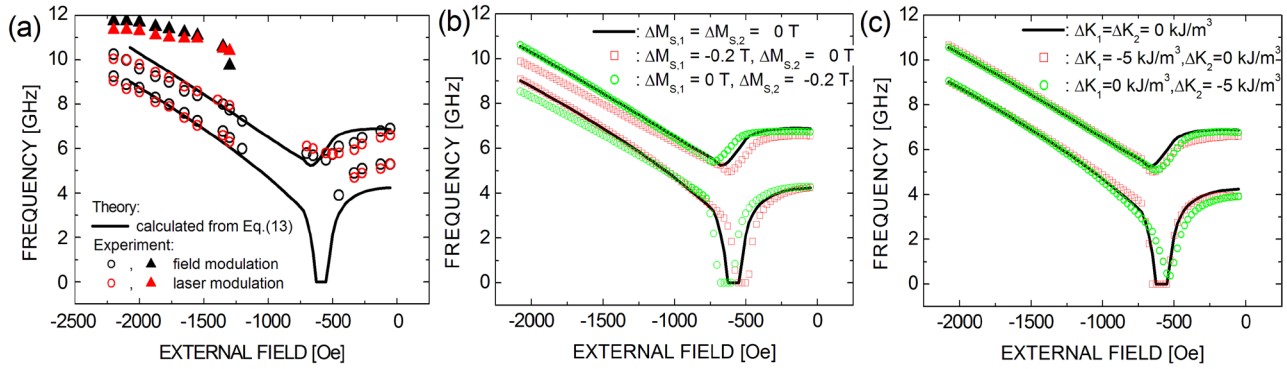

Figure 3. The resonance frequencies versus external field: (a) the theoretical curves (solid lines) calculated from equation (13), compared to experimental points in the field modulation (black points) and laser modulation (red points) technique, (b) theoretical resonance frequency shift due to a temperature dependence of the saturation magnetizations as well as (c) due to temperature dependence of the magnetocrystalline anisotropy.

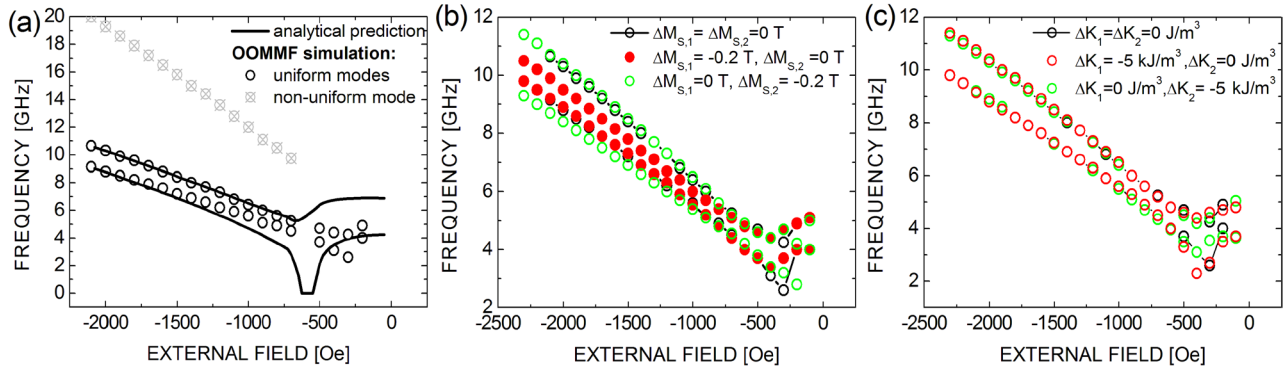

Figure 4. Micromagnetic simulations: (a) resonance modes versus external field (circles) qualitatively compared to the macrospin predictions (black solid lines), (b) resonance frequencies shifts due to temperature-induced decrease of magnetization and (c) due to temperature-induced decrease of magnetocrystalline anisotropy.

at the tip of which a gold wire was soldered. The wire would rub the surface of the electrodeposited membrane until contact was established. This allowed us to measure magnetoresistance as a function of magnetic field (see figure 2) and then to drive the ferromagnetic resonance with microwave currents at 4–10 GHz. In the conventional detection mode, a field modulation with a peak-to-peak amplitude of 27 Oe was used. For the thermal experiment, no field modulation was applied. The laser light was guided in an optical fiber, the end of which was lodged in a hole at the side of the SMA connector, pointing toward the membrane inside it. The temperature rise under laser light was calibrated by thermoelectric measurements and amounts to about 5 K [19]. In both cases, the rectified signal (through the spin diode effect) was detected by a standard lock-in technique, using the drive of the field modulation coil or of the laser diode as reference.

4. Results and discussion

The nanowires under consideration consist of two cobalt ferromagnetic layers separated by a non-magnetic Cu spacer. Because of the electrochemical deposition method used to fabricate the nanowires, the thin layer in an individual nanowire may have slightly different magnetic properties than the corresponding thick layer. This is due to the presence of copper atoms that are co-deposited in the magnetic layers. As a consequence, the thinner layer can be expected to be more affected by the non-magnetic impurities. For our purposes, we assume the following magnetic parameters of both layers: $M_{S,2} = 1.4$ T, $K_2 = 25$ kJ m^{-3} and $M_{S,1} = 1.2$ T, $K_1 = 15$ kJ m^{-3}. Apart from this, the thicknesses of thick and thin layers were chosen as $d_2 = 12$ nm and $d_1 = 5$ nm, respectively. In turn, for the thickness of the non-magnetic Cu spacer, we assumed 25 nm, for which the mean values of dipolar fields in the thick ($\bar{H}_{dip,1}$) and thin ($\bar{H}_{dip,2}$) layers were 74 Oe and 177 Oe, respectively. In the experiment, the nanowires are deposited into the nanopores of a polycarbonate mambrane. Thus, the external magnetic field applied in the plane of the whole membrane may not be applied exactly in the plane of nanowire's cross section. In other words, the nanowire axis may not be collinear with the membrane axis, and they may form an angle of up to 40 degrees. Similarly, the external field orientation may not be exactly perpendicular to the easy axes of the magnetic layers, but

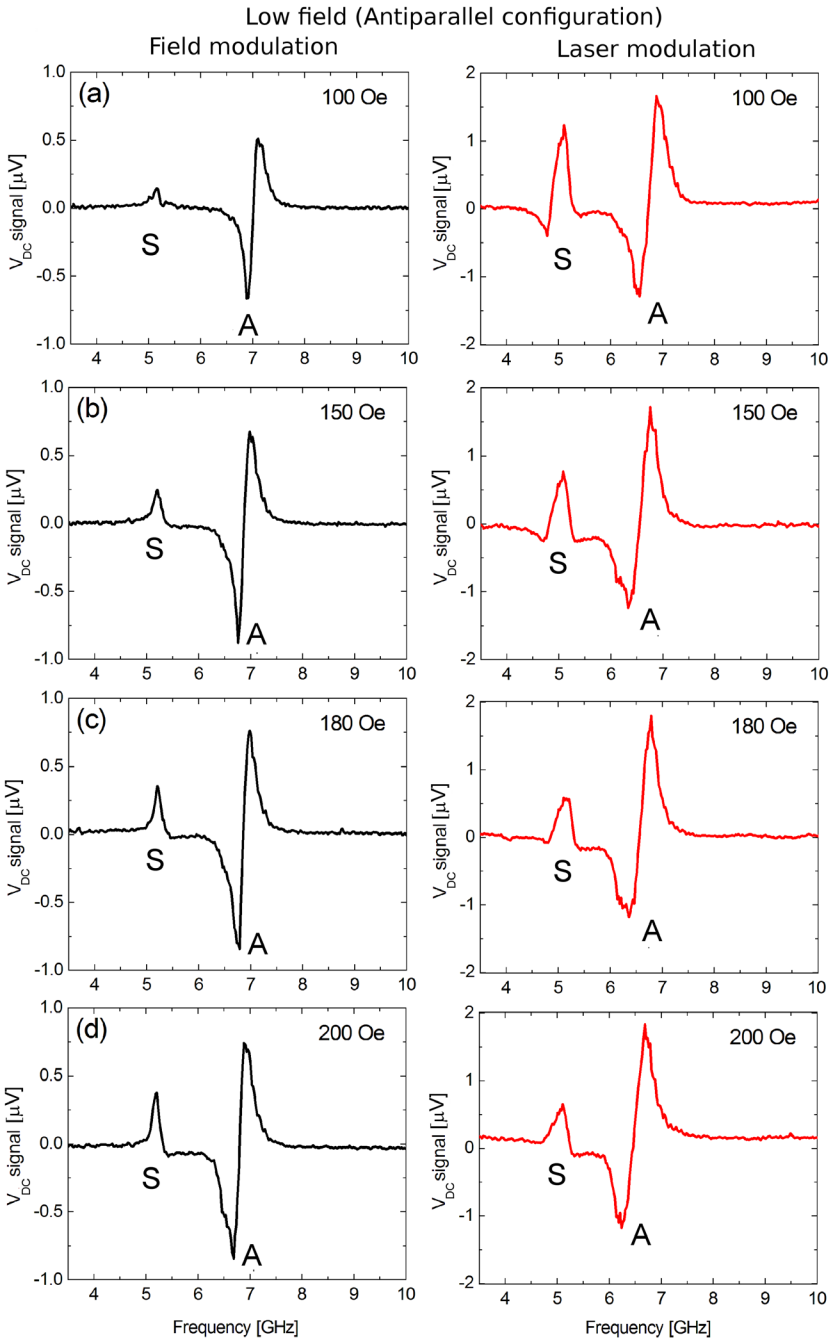

Figure 5. Experimental lineshapes measured at low magnetic fields (antiparallel configuration of $\boldsymbol{M_1}$ and $\boldsymbol{M_2}$) with the two modulation techniques: magnetic field modulation (black lines on the left side) and laser modulation (red lines on the right side). Letters 'S' and 'A' stand for symmetric and antisymmetric lineshape, respectively.

it may deviate from 90 degrees. The polar and azimuthal angles describing the orientation of the external magnetic field, Ψ and β, have been set as $\Psi = 72°$ and $\beta = 63°$ to ensure a good agreement with the experimentally measured FMR dispersion relation as well as to obtain a non-zero angle between the magnetic moments even at high external magnetic fields.

4.1. Dispersion relation

In figure 3(a) we compare the theoretical FMR dispersion relation for the modes determined from equation (13) with the experimental measurements done with both FMR detection schemes: field modulation and temperature modulation. In general, there are two ways in which laser heating can affect the sample. One of them is a laser-induced decrease in the magnetocrystalline anisotropy, and the second one is a laser-induced decrease in the magnetization according to the Bloch's law applied to nanostructures [30].

As one can see in figures 3(b) and (c), the influence of the increase in temperature on resonance frequencies is rather small and only a slight shift of the frequency can be noticed. Interestingly, a similar slight shift can be observed also in the experimentally determined dispersion relations as well

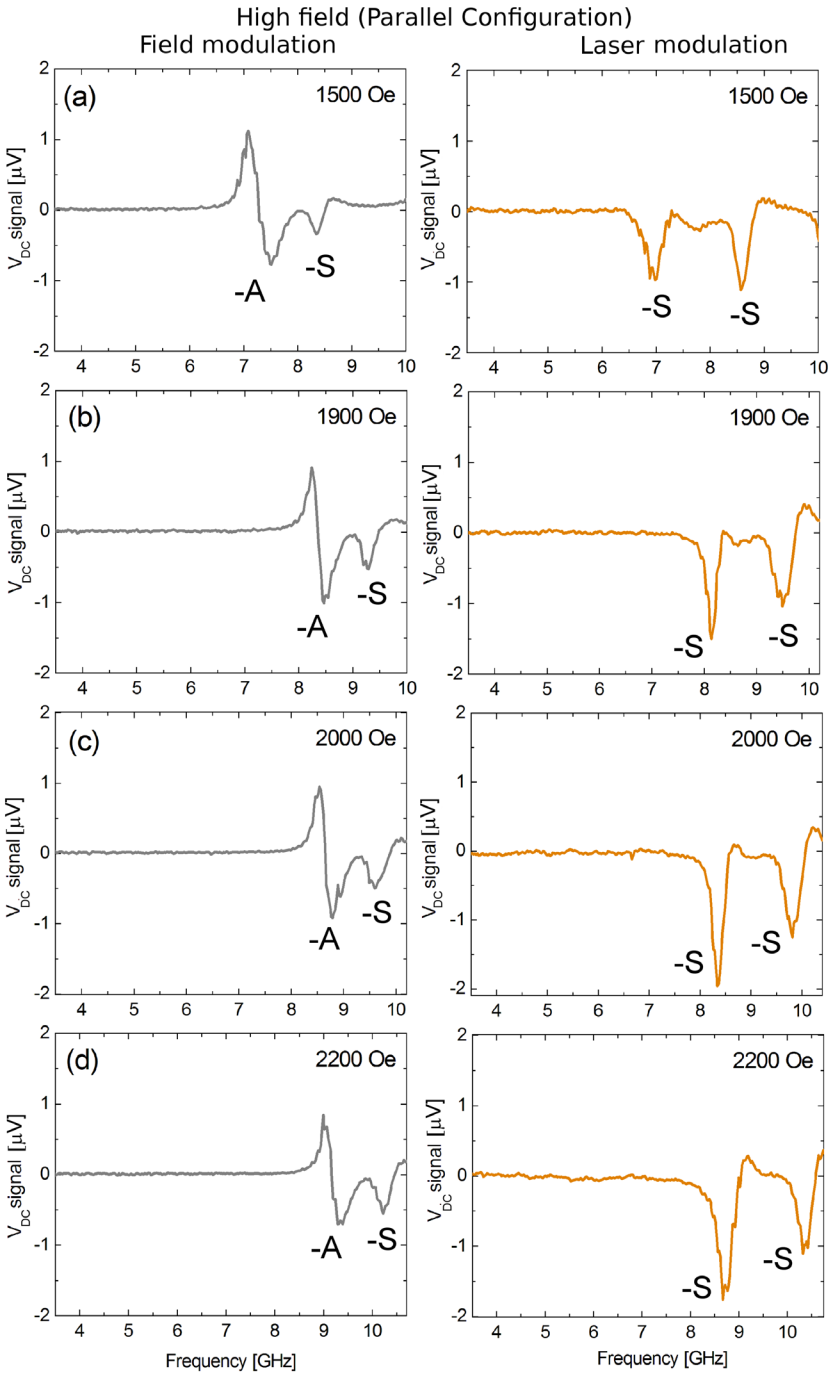

Figure 6. Experimental lineshapes measured at high magnetic fields (parallel configuration of $\boldsymbol{M_1}$ and $\boldsymbol{M_2}$) with the two modulation techniques: magnetic field modulation (grey lines on the left side) and laser modulation (orange lines on the right side). Letters 'S' and 'A' stand for symmetric and antisymmetric lineshape, respectively.

as in those obtained from the micromagnetic simulations shown in figures 3(a) and 4(b) and (c). The simulations were performed with the use of OOMMF package [31] with our custom software [32, 33]. The LLGS equation was solved numerically in each $2\times2\times1$ nm simulation cell for magnetic parameters identical to those utilized in the analytical calculations described above. After the initial magnetization relaxation, a small magnetic pulse of 10 Oe was used to excite both ferromagnetic layers and their magnetization response was subjected to a Fast Fourier transform (FFT) from which we obtained the resonance frequencies of the system.

The analytical model based on the macrospin approximation predicts only two separate resonance modes. However, the experimental observations and micromagnetic simulations of the frequency versus magnetic field dependence indicate the presence of a third mode at high magnetic

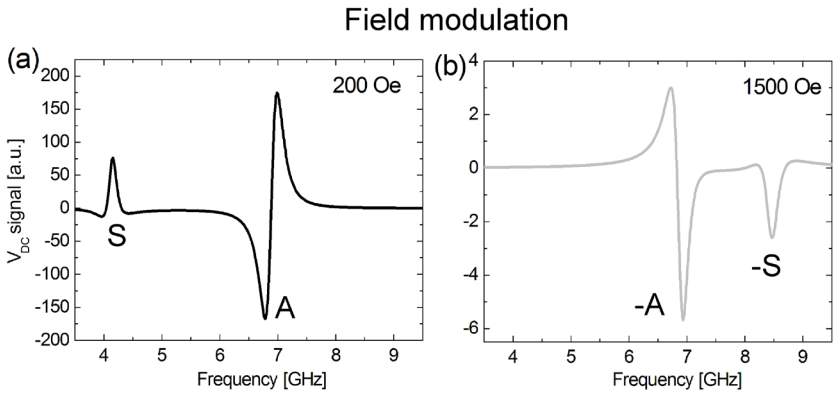

Figure 7. Macrospin simulation of the V_{DC} lineshape with field modulation calculated at external field 200 Oe (a) and 1500 Oe (b) (for phase shifts, see text).

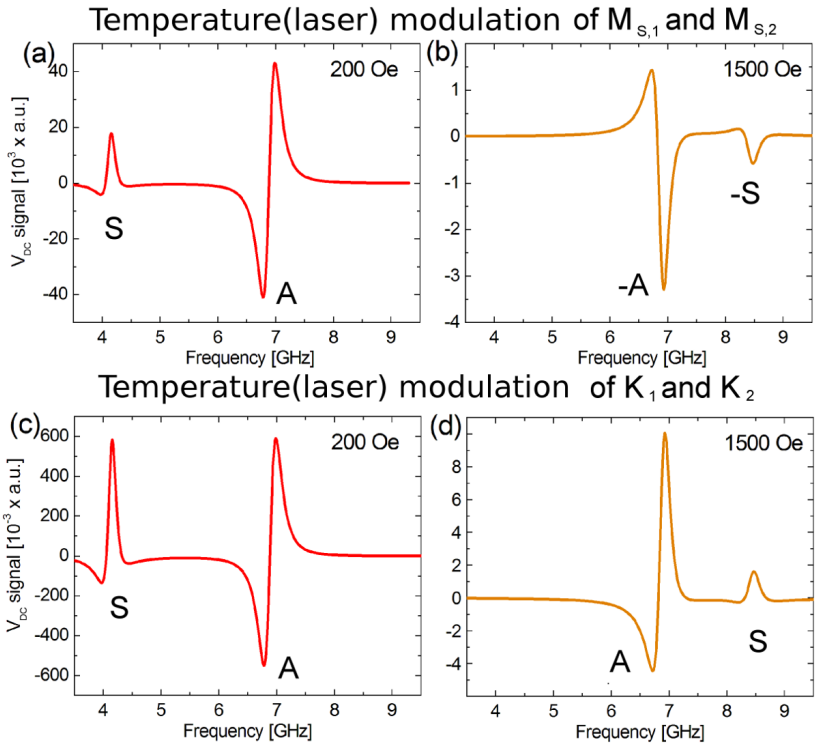

Figure 8. Macrospin simulations of the V_{DC} lineshapes with temperature modulations of the magnetizations (a) and (b) and anisotropies (c) and (d), calculated at external field 200 Oe and 1500 Oe. The phase shift and other parameters are the same as in the field modulation technique.

fields, see figures 3(a) and 4(a). This additional mode may be related to a more complex dynamics in the system, possibly due to presence of magnetic inhomogeneities at the boundaries of both magnetic layers or to spin-wave-like excitations [34]. However, since we focus in this paper on the influence of different modulation techniques on the SDE lineshapes of the FMR modes, the non-uniform mode weakly coupled to them and not affecting their symmetries [35] remains beyond the scope of this paper. Thus, in the following we will discuss the FMR (uniform) modes only, for which the experimental, macrospin and micromagnetic approaches are consistent, see figures 3 and 4.

4.2. Lineshapes in both field and laser modulation techniques

Equation (16) for the V_{DC} signal has to be modified due to the measurement technique used in the experiment. This technique is commonly known as the field-modulated FMR [34]. Furthermore, we explored here the possibility to apply temperature modulation, as a simple laser diode is sufficiently powerful to modulate the temperature of a nanowire [19]. The V_{DC} signal in both techniques can be expressed simply as:

$$V_{DC,H} = \frac{dV_{DC}}{dH_m}\delta H_m \tag{19}$$

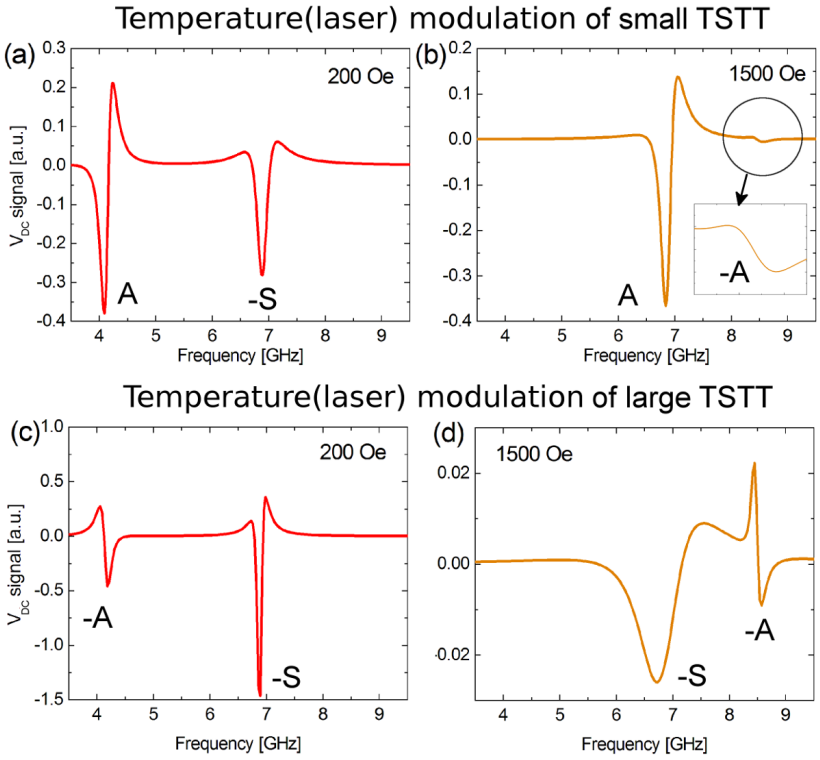

Figure 9. Macrospin simulation of the V_{DC} lineshapes with modulation of small and large TSTT calculated at low field (200 Oe) (a)–(c) and high field (1500 Oe) (b)–(d). The phase shifts and other parameters are the same as in the field modulation mode. Inset: zoom of the small second peak from panel (b).

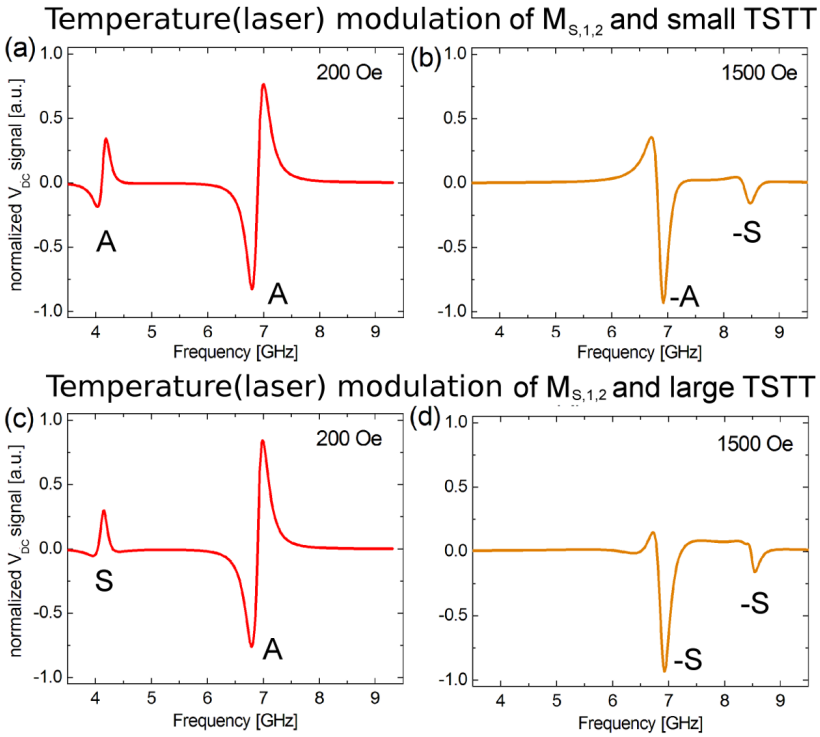

Figure 10. Macrospin simulation of the V_{DC} lineshapes with contribution from temperature modulation of magnetizations ($\boldsymbol{M}_{1,2}$) and (a) and (b) small and (c) and (d) large TSTT calculated at low (200 Oe) and high (1500 Oe) fields. The phase shifts and other parameters are the same as in the field modulation mode.

and

$$V_{DC,T} = \frac{dV_{DC}}{dT}\delta T, \tag{20}$$

where δH_m and δT denote the amplitude of modulation field and the amplitude of the temperature change, respectively. In this model, V_{DC} signal does not depend on the temperature explicitly. However, it is possible to introduce temperature-dependent anisotropy and magnetization according to Bloch's law. Moreover, the temperature gradient may induce a flow of spin current leading to TSTT acting on a magnetic layer [20]. Thus, in the temperature modulation technique, we may rewrite equation (20) as:

$$V_{DC,T} = \sum_{i=1}^{2}\left(\frac{\partial V_{DC}}{\partial M_{S,i}}\frac{\partial M_{S,i}}{\partial T} + \frac{\partial V_{DC}}{\partial K_i}\frac{\partial K_i}{\partial T}\right)\delta T + \sum_{i=2}^{2}\frac{\partial V_{DC}}{\partial \tau_{\parallel,i}}\frac{\partial \tau_{\parallel,i}}{\partial \Delta T}\delta\Delta T \tag{21}$$

where ΔT is temperature gradient between magnetic layers, and the quantity $\frac{\partial \tau_{\parallel,i}}{\partial \Delta T}$ refers to as thermal torkance of the layer i. In the following $V_{DC,H}$ and $V_{DC,T}$ will be denoted simply as V_{DC}, if not stated otherwise.

The experimental V_{DC} spectra corresponding to the uniform modes from figure 3(a) and measured at several values of magnetic field are presented in figures 5 and 6. As one can note, the symmetry of the peaks in the field modulation and laser modulation techniques is the same at low fields. On the contrary, the symmetry of the peaks at high fields is different in the two modulation techniques. This observation raises the question as to why the modulation technique affects the lineshape symmetry. This problem is now analyzed in detail. For further theoretical analysis we choose two values of magnetic field, 200 Oe and 1500 Oe, referred to as low and high field (or antiparallel and pararallel configuration) respectively.

The lineshape of the V_{DC} spectrum is very sensitive to the phase shifts and to the origin of the driving force. Due to coupling of the layers by both the dipolar field and STT effects, the symmetries of both peaks cannot be considered separately. Instead, we look at the simultaneous dynamics of both ferromagnetic layers, and consider the symmetry of the whole spectrum. For example, a change of the phase shifts for the magnetization dynamics in one layer has a significant influence on the lineshape of the two resonant peaks, as they are linked to each layers.

Let us start the analysis of lineshapes with choosing the phase shifts $\Psi_{1,2,3,4}$ to obtain agreement between the theoretical lineshapes and the experimental ones in the field modulation technique. According to equation (19), the output V_{DC} voltage is a derivative with respect to the modulating magnetic field. In figure 7 we plot the field modulated V_{DC} signal at low and high external magnetic fields. The phase shifts Ψ_{1-4} were chosen as follows: $\Psi_2 = 160°$ and $\Psi_4 = 240°$ at 200 Oe and $\Psi_2 = 90°$ and $\Psi_4 = 60°$ at 1500 Oe. The phase shifts $\Psi_{1,3} = 90°$ were fixed at both fields. As one can conclude from the figure 7, the lineshape symmetries agree well with the experimental ones at both low and high fields.

Table 1. Summary of the experimental and theoretical lineshape symmetries in field- and temperature modulation technique at low (200 Oe) and high field (1.5 kOe). S(AS) denotes symmetric(antisymmetric) peak. The sign − corresponds to the peak with negative extremum in the case of symmetric peak, and the first negative extremum in the case of antisymmetric peak. The theoretical results are bolded when converge to the experimental ones.

	Symmetry of peaks	
Type of V_{DC} modulatation	Low field	High field
Experimental:		
Field modualtion	**S, A**	**− A, −S**
Temperature(laser) modulation	**S, A**	**− S, −S**
Theoretical:		
Field modulation (H_m)	**S, A**	**− A, −S**
Temperature(laser) modulation of:		
$M_{S,1,2}$	S, A	−A, −S
$K_{1,2}$	S, A	A, S
small TSTT	A, −S	A, −A
large TSTT	−A, −S	−S, −A
$M_{S,1,2}$ + small TSTT	A, A	−A, −S
$M_{S,1,2}$ + large TSTT	**S, A**	**− S, −S**

The other modulation technique used is the laser modulation one. In this method, the rectified signal V_{DC} is determined as a derivative with respect to the amplitude of the temperature modulation (induced by laser). First, we consider the temperature modulation of magnetizations ($M_{S,i}$) and magnetic anisotropies (K_i), when $\Delta T = 0$. According to equation (21), in order to calculate properly the V_{DC} signal in the laser modulation technique one has to know the temperature dependence of $M_{S,i}$ and K_i. Here, we omit this problem and assume that the saturation magnetization and anisotropies decrease with increasing temperature, i.e. their derivatives are negative. The modulation strength (e.g. $\frac{dK}{dT}$, $\frac{dM_S}{dT}$) does not change the symmetry of lineshapes: stronger modulation enhances the peak amplitudes only. Therefore, as long as our objective is to show how the change of modulation technique influences lineshapes, we may not consider the magnitude of the derivatives. For the sake of simplicity we assume that the changes in the magnetic parameters (saturation magnetization and anisotropy constants) in both layers are the same and that the phase shifts are the same as those assumed in the case of the field modulation technique.

In figure 8 we show the V_{DC} signal in the laser modulation technique. We consider two cases: the first case is the

modulation of saturation magnetizations, while the second one is the modulation of anisotropies. Comparing to the field modulation (figure 7), there is no significant change of the lineshape symmetries at low and high field in the first case. The first peak at high field becomes slightly more symmetric than in the case of the field modulation, but still it can be clearly referred to as antisymmetric peak. Also, one can notice a small decrease in amplitude of the second peak at high field. However, one should bear in mind that the amplitude depends on the derivative $\frac{\partial M_{S,i}}{\partial T}$ and modulation temperature δT as well. Thus, the real amplitude of the signal will be different than that shown in this figure. On the contrary, the temperature modulation of the anisotropies affects the lineshape, particularly the sign of the spectrum at high field (see figure 8(d)). Furthermore, in contrast to the field modulation, the first peak at low field is much higher with respect to the second one (see figures 7(a) and 8(d)). Similarly as in the case of temperature modulation of $M_{S,i}$, the first peak at high field seems to be slightly more symmetric than in the field modulation technique, however its shape is still mostly antisymmetric. Thus, in terms of lineshape symmetries, one can say that at low field the symmetry of the lineshape is conserved in both field and temperature modulation. Furthermore, the lineshape is more affected by temperature-induced anisotropy modulation than by saturation magnetization modulation at high fields.

We now turn to the question whether the laser-induced temperature gradient gives rise to a significant heat-driven spin torque (TSTT). We assume that the top and bottom layers have been heated up by the laser light in such a way that temperature gradient (ΔT) has been generated along the nanowire. Thus the warmer magnetic layer may act as a source of spin polarized heat current and TSTT that influences the magnetization dynamics within the cooler one. In figure 9 we can see how such a type of modulation influences the lineshape of the V_{DC} signal.

As one can see, the TSTT modulation changes the symmetry of both peaks at low and high field: symmetric (antisymmetric) peaks in field modulation become antisymmetric (symmetric) peaks in the TSTT modulation. Moreover, the shape of symmetric(antisymmetric) peaks depends on the TSTT magnitude. This feature is reflected in figure 9 where two cases are shown. In the first one (figures 9(a) and (b)), the V_{DC} signal was modulated just by a small TSTT (of order of nJ per $m^2 \times 1$ K) due to change of the temperature gradient ($\delta\Delta T$). In the second case (figures 9(c) and (d)), we assumed additionaly that V_{DC} is modulated in the the presence of stationary non-zero temperature gradient (ΔT_0) that is large enough to modify the effective damping of the magnetic layers. In the case of small TSTT, one can see that the second peak at high field is suppresed. Despite of its very small amplitude, its antisymmetric lineshape may be identified (see inset in figure 9(b)). The larger magnitude of STT affects the amplitude as well as the sign and width of V_{DC} peaks. Such a behaviour is related to increase(or decrease) of effective damping due to TSTT effect [25]. Considering the results on temperature modulation (of $M_{S,i}$, K_i or TSTT), one can see that these results clearly differ from those observed experimentally. One of the most apparent reasons for this is that temperature-related phenomena cannot be considered separatly, since all of them may contribute to the final output spectrum in a general case.

In order to illustrate this issue and to obtain more realistic lineshapes, we considered the coexistence and competition of the two effects: temperature modulations of TSTT and $M_{S,1,2}$. First, we normalized the spectra amplitudes from figures 8(a) and (b) and 9(a)–(d) to 1.0, so that their maximum(or minimum) values were set to 1 (or -1). Next, we added normalized M_S and TSTT temperature-modulated spectra with different weights, accounting for their different contributions to the overall spectra. In our case weights were 0.8 and 0.2 for M_S and TSTT modulation respectively. The results are shown in figure 10. One can see that lineshapes of such combined spectra are more similar to the experimental ones, than when two modulation effects are considered separetely. When considering small TSTT (figures 10(a) and (b)), one can see that first peak has an important antisymmetric contribution, at both low and high fields. However, the increase of the TSTT magnitude makes these two peaks more symmetric (figures 10(c) and (d)), while the other ones remain unchanged. Despite of the difference in calculated and experimental peak amplitudes, peak symmetries agree well in this case. Thus, we can conclude that assuming a TSTT effect (but still dominated by temperature-related M_S modulation effect) results in better agreement between theoretical and experimental lineshape symmetries.

5. Conclusions

In this paper we discussed the important factors pertaining to the SDE measurements in GMR nanowires with two magnetic layers coupled by both dipolar field and STT effects. First, we showed that our analytical model is able to describe experimentally observed FMR (uniform) modes in this system. Our results were supported by micromagnetic simulations as well. Next, we calculated the SDE lineshapes corresponding to two different modulations techniques, field and temperature(laser) modulation. We compared our analytical predictions with experimental SDE spectra. We found that experimental lineshapes can be successfully analysed by the present model. Moreover, we discussed the influence of the modulation method on symmetry of the resonance peaks, and showed that the modulation technique can be distinguished by the effect they have on the SDE lineshapes. We considered different contributions to the SDE spectra coming from heat-related modulation of magnetizations, anisotropies and TSTTs. Our results are summarized in table 1.

We showed that the temperature-modulated magnetic anisotropy influences the SDE lineshapes more than the temperature-modulated magnetization. However, a possible competition of different heat-related phenomena makes the lineshape analysis in laser modulation technique much more complex than in the case of field modulation technique. The

presented model may be used to investigate spin-diode spectra in different GMR or TMR spintronic/caloritronic structures, where dynamics of two coupled magnetic layers together with heat-related phenomena has to be taken into consideration.

Acknowledgments

The research was financed by NANOSPIN Grant No. PSPB-045/2010 from Switzerland through the Swiss Contribution. Numerical calculations were supported in part by PL-GRID infrastructure. JCh acknowledges funding from PhD scholarship no. 2017/24/T/ST3/00009 by National Science Center, Poland. TS and PO acknowledge the grant SpinOrbitronics No. 2016/23/B/ST3/01430 by National Science Center, Poland. PO acknowledges financial support from Dekaban Fund at the University of Michigan where the work was partially done.

Appendix. Coupled LLGS equation in polar coordinates

In general case, the effective fields in equation (3), i.e. $\boldsymbol{H}_{\mathrm{eff},1}$ and $\boldsymbol{H}_{\mathrm{eff},2}$, can be written in the form: $\boldsymbol{H}_{\mathrm{eff},1}$ and $\boldsymbol{H}_{\mathrm{eff},2}$, can be written in the form:

$$\boldsymbol{H}_{\mathrm{eff},1} = -\nabla_{\theta,\phi}U + H_{\mathrm{oe}}\hat{\boldsymbol{e}}_{\boldsymbol{\phi}}, \tag{A.1a}$$

$$\boldsymbol{H}_{\mathrm{eff},2} = -\nabla_{\Lambda,\Omega}U + H_{\mathrm{oe}}\hat{\boldsymbol{e}}_{\boldsymbol{\Omega}}, \tag{A.1b}$$

where U is the total magnetic energy of the system, while H_{oe} is the circular Oersted field generated by the current. Amplitude of the Oersted field, in principle, depends on the distance from the z axis (see figure 1). However, in the spirit of macrospin model we take into account the strength of the field averaged along the radius of the nanowire, in the following way:

$$H_{oe} = \frac{1}{R}\int_0^R H_r(r)dr \tag{A.2}$$

where R denotes radius of the nanowire, and $H_r(r)$ is local Oersted field at distance r from the axis of nanowire. In the spherical coordinate system, the in-plane and out-of-plane STT components of $\boldsymbol{\tau}_1$ may be written as functions of the angles $\theta, \phi, \Lambda, \Omega$ as

$$\begin{aligned}\boldsymbol{\tau}_{\parallel,1} = \tau_{\parallel,1}\,[&\hat{\boldsymbol{e}}_{\boldsymbol{\theta}}(-\cos\Lambda\sin\theta + \cos\theta\cos(\phi-\Omega)\sin\Lambda)\\ &-\hat{\boldsymbol{e}}_{\boldsymbol{\phi}}\sin\Lambda\sin(\phi-\Omega)]\,,\end{aligned} \tag{A.3a}$$

$$\begin{aligned}\boldsymbol{\tau}_{\perp,1} = \tau_{\perp,1}\,[&-\hat{\boldsymbol{e}}_{\boldsymbol{\phi}}(\cos\Lambda\sin\theta - \cos\theta\cos(\phi-\Omega)\sin\Lambda)\\ &+\hat{\boldsymbol{e}}_{\boldsymbol{\theta}}\sin\Lambda\sin(\phi-\Omega)]\,,\end{aligned} \tag{A.3b}$$

and similarly, the STT components acting on the thick layer may be expressed as

$$\begin{aligned}\boldsymbol{\tau}_{\parallel,2} = \tau_{\parallel,2}\,[&-\hat{\boldsymbol{e}}_{\boldsymbol{\Lambda}}(\cos\theta\sin\Lambda - \cos\Lambda\cos(\phi-\Omega)\sin\theta)\\ &+\hat{\boldsymbol{e}}_{\boldsymbol{\Omega}}\sin\theta\sin(\phi-\Omega)]\,,\end{aligned} \tag{A.4a}$$

$$\begin{aligned}\boldsymbol{\tau}_{\perp,2} = \tau_{\perp,2}\,[&\hat{\boldsymbol{e}}_{\Omega}(-\cos\theta\sin\Lambda + \cos\Lambda\cos(\phi-\Omega)\sin\theta)\\ &-\hat{\boldsymbol{e}}_{\boldsymbol{\Lambda}}\sin\theta\sin(\phi-\Omega)]\,,\end{aligned} \tag{A.4b}$$

where $\hat{\boldsymbol{e}}_{\boldsymbol{\theta}}, \hat{\boldsymbol{e}}_{\boldsymbol{\Lambda}}, \hat{\boldsymbol{e}}_{\boldsymbol{\phi}}, \hat{\boldsymbol{e}}_{\boldsymbol{\Omega}}$ are unit vectors associated with the polar θ, Λ and azimuthal ϕ, Ω angles, respectively. The Landau–Lifshitz–Gilbert–Slonczewski (LLGS) equations written in spherical coordinates lead to the following equations for the azimuthal and polar angles:

$$\begin{pmatrix}\dot{\theta}\\ \dot{\phi}\\ \dot{\Lambda}\\ \dot{\Omega}\end{pmatrix} = \begin{pmatrix}
\frac{\gamma}{(1+\alpha_1^2)M_{S,1}}\Big\{-\frac{1}{\sin\theta}\frac{\partial U}{\partial\phi} - \alpha_1\frac{\partial U}{\partial\theta} - [\cos\Lambda\sin\theta - \cos\theta\sin\Lambda\cos(\phi-\Omega)](\tau_\parallel + \alpha_1\tau_\perp)\\ \quad -[\sin\Lambda\sin(\phi-\Omega)](\alpha_1\tau_\parallel - \tau_\perp) + M_{S,1}H_{oe}\Big\}\\
\frac{\gamma}{(1+\alpha_1^2)M_{S,1}}\Big\{\frac{1}{\sin\theta}\frac{\partial U}{\partial\theta} - \frac{\alpha_1}{\sin^2\theta}\frac{\partial U}{\partial\phi} + \frac{1}{\sin\theta}[\cos\Lambda\sin\theta - \cos\theta\sin\Lambda\cos(\phi-\Omega)](\alpha_1\tau_\parallel - \tau_\perp)\\ \quad -\frac{1}{\sin\theta}[\sin\Lambda\sin(\phi-\Omega)](\tau_\parallel + \alpha_1\tau_\perp) + \frac{\alpha_1 M_{S,1}H_{Oe}}{\sin\theta}\Big\}\\
\frac{\gamma}{(1+\alpha_2^2)M_{S,2}}\Big\{-\frac{1}{\sin\Lambda}\frac{\partial U}{\partial\Omega} - \alpha_2\frac{\partial U}{\partial\Lambda} + [-\sin\Lambda\cos\theta + \sin\theta\cos\Lambda\cos(\phi-\Omega)](\tau_{\parallel,2} + \alpha_2\tau_{\perp,2})\\ \quad +[\sin\Lambda\sin(\phi-\Omega)](\tau_{\perp,2} + \alpha_2\tau_{\parallel,2}) + M_{S,2}H_{oe}\Big\}\\
\frac{\gamma}{(1+\alpha_2^2)M_{S,2}}\Big\{\frac{1}{\sin\Lambda}\frac{\partial U}{\partial\Lambda} - \frac{\alpha_2}{\sin^2\Lambda}\frac{\partial U}{\partial\Omega} - \frac{1}{\sin\Lambda}[\sin\Lambda\cos\theta - \sin\theta\cos\Lambda\cos(\phi-\Omega)](\tau_{\perp,2} - \alpha_2\tau_{\parallel,2})\\ \quad +\frac{1}{\sin\Lambda}[\sin\theta\sin(\phi-\Omega)](\tau_{\parallel,2} - \alpha_2\tau_{\perp,2}) + \frac{\alpha_2 M_{S,2}H_{Oe}}{\sin\Lambda}\Big\}
\end{pmatrix}. \tag{A.5}$$

ORCID iDs

Piotr Ogrodnik https://orcid.org/0000-0002-4907-3409
Tomasz Stobiecki https://orcid.org/0000-0001-7380-2897

References

[1] Tulapurkar A, Suzuki Y, Fukushima A, Kubota H, Maehara H, Tsunekawa K, Djayaprawira D, Watanabe N and Yuasa S 2005 *Nature* **438** 339

[2] Sankey J, Braganca P, Garcia A, Krivorotov I, Buhrman R and Ralph D 2006 *Phys. Rev. Lett.* **96** 227601
[3] Sankey J, Cui Y T, Sun J, Slonczewski J, Buhrman R and Ralph D 2007 *Nat. Phys.* **4** 67
[4] Kubota H *et al* 2007 *Nat. Phys.* **4** 37
[5] Locatelli N, Cros V and Grollier J 2014 *Nat. Mater.* **13** 11
[6] Ziętek S, Ogrodnik P, Frankowski M, Chęciński J, Wiśniowski P, Skowroński W, Wrona J, Stobiecki T, Żywczak A and Barnaś J 2015 *Phys. Rev.* B **91** 014430
[7] Harder M, Gui Y and Hu C M 2016 *Phys. Rep.* **661** 1
[8] Jenkins A *et al* 2016 *Nat. Nanotechnol.* **11** 360–4
[9] Ziętek S, Ogrodnik P, Skowroński W, Wiśniowski P, Czapkiewicz M, Stobiecki T and Barnaś J 2015 *Appl. Phys. Lett.* **107** 122410
[10] Layadi A 2004 *Phys. Rev.* B **69** 144431
[11] Layadi A 2015 *AIP Adv.* **5** 057113
[12] Layadi A and Artman J 1990 *J. Magn. Magn. Mater.* **92** 143
[13] Kozioł-Rachwał A *et al* 2017 *J. Magn. Magn. Mater.* **424** 189
[14] Moriyama T, Finocchio G, Carpentieri M, Azzerboni B, Ralph D C and Buhrman R A 2012 *Phys. Rev.* B **86** 060411
[15] Natarajan K, Arumugam B and Rajamani A 2016 *J. Magn. Magn. Mater.* **410** 210
[16] Bell R, Hu J and Victora R 2017 *AIP Adv.* **7** 055929
[17] Slonczewski J C 1996 *J. Magn. Magn. Mater.* **159** L1
[18] Hatami M, Bauer G E W, Zhang Q and Kelly P J 2007 *Phys. Rev. Lett.* **99** 066603
[19] Gravier L, Fábián A, Rudolf A, Cachin A, Hjort K and Ansermet J P 2004 *Meas. Sci. Technol.* **15** 420
[20] Luc D and Waintal X 2014 *Phys. Rev.* B **90** 144430
[21] Choi G M, Moon C H, Min B C, Lee K J and Cahill D G 2015 *Nat. Phys.* **11** 576
[22] Fitoussi L, Vetro F A, Caspers C, Gravier L, Yu H and Ansermet J P 2015 *Appl. Phys. Lett.* **106** 162401
[23] Bose A *et al* 2016 *Appl. Phys. Lett.* **109** 032406
[24] Pushp A, Phung T, Rettner C, Hughes B P, Yang S H and Parkin S S P 2015 *Proc. Natl Acad. Sci. USA* **112** 6585
[25] Zhang Z, Bai L, Chen X, Guo H, Fan X, Xue D, Houssameddine D and Hu C M 2016 *Phys. Rev.* B **94** 064414
[26] Sato M and Ishii Y 1989 *J. Appl. Phys.* **66** 983
[27] Boulle O, Cros V, Grollier J, Pereira L, Deranlot C, Petroff F, Faini G, Barnaś J and Fert A 2007 *Nat. Phys.* **3** 492
[28] Biziere N, Mure E and Ansermet J P 2009 *Phys. Rev.* B **79** 012404
[29] Murè E, Biziere N and Ansermet J P 2010 *J. Magn. Magn. Mater.* **322** 1443
[30] Cojocaru S, Naddeo A and Citro R 2014 *Europhys. Lett.* **106** 17001
[31] Donahue M J and Porter D G 1999 *OOMMF User's Guide* (Gaithersburg, MD: US Department of Commerce, Technology Administration, National Institute of Standards and Technology)
[32] Frankowski M, Czapkiewicz M, Skowroński W and Stobiecki T 2014 *Physica B: Condens. Matter.* **435** 105
[33] Chęciński J and Frankowski M 2016 *Comput. Phys. Commun.* **207** 487
[34] Gonçalves A, Barsukov I, Chen Y J, Yang L, Katine J and Krivorotov I 2013 *Appl. Phys. Lett.* **103** 172406
[35] Frankowski M, Chęciński J, Skowroński W and Stobiecki T 2017 *J. Magn. Magn. Mater.* **429** 11